physchem

MDPI

Article

Morphological Engineering of Battery-Type Cobalt Oxide Electrodes for High-Performance Supercapacitors

Boddu Haritha [1], Mudda Deepak [1], Obili M. Hussain [1,*] and Christian M. Julien [2,*]

[1] Thin Film Laboratory, Department of Physics, Sri Venkateswara University, Tirupati 517502, India; harithathinfilms@gmail.com (B.H.); deepakmudda7@gmail.com (M.D.)
[2] Institut de Minéralogie, de Physique des Matériaux et de Cosmologie (IMPMC), Sorbonne Université, 4 Place Jussieu, 75252 Paris, France
* Correspondence: hussainsvu@gmail.com (O.M.H.); christian.julien@sorbonne-universite.fr (C.M.J.)

Abstract: Nanomaterials have attracted significant attention in recent decades for their diverse applications, including energy storage devices like supercapacitors. Among these, cobalt oxide (Co_3O_4) nanostructures stand out due to their high theoretical capacitance, unique electrical properties, and tunable morphology. This study explores the hydrothermal synthesis of Co_3O_4, revealing that the molar ratio of cobalt nitrate to potassium hydroxide significantly influences the morphology, crystal structure, and electrochemical performance. An optimized 1:1 molar ratio (COK 11) yielded well-defined cubic nanostructures with uniform elemental distribution, as confirmed by SEM, TEM, and EDS analyses. Structural characterization through XRD, XPS, and FTIR validated the formation of the Co_3O_4 spinel phase with distinctive lattice and surface oxygen features. Electrochemical property analysis demonstrated the superior performance of the COK 11 electrode, achieving a high specific capacity of 825 $\pm$ 3 F/g at a current density of 1 A/g, a rate capability of 56.88%, and excellent cycle stability of 88% at 3 A/g after 10,000 cycles. These properties are attributed to the nano-cubic morphology and interconnected porosity, which enhanced ion transport and active surface area. This study highlights the importance of synthesis parameters in tailoring nanomaterials for energy storage, establishing COK 11 as a promising candidate for next-generation high-performance supercapacitor applications.

Keywords: Co_3O_4 nanocubes; hydrothermal method; specific capacitance; morphology; supercapacitors

Academic Editor: Sergei Manzhos

Received: 16 December 2024
Revised: 5 March 2025
Accepted: 12 March 2025
Published: 14 March 2025

Citation: Haritha, B.; Deepak, M.; Hussain, O.M.; Julien, C.M. Morphological Engineering of Battery-Type Cobalt Oxide Electrodes for High-Performance Supercapacitors. *Physchem* **2025**, *5*, 11. https://doi.org/10.3390/physchem5010011

1. Introduction

Nanomaterials have been used in various applications in recent decades, including microelectronic circuits, sensors, energy storage devices, piezoelectric devices, and fuel cells. In particular, they have sparked widespread interest in supercapacitor applications owing to their large surface area, unique electrical characteristics, and tunable morphology. Material characteristics at the nanoscale are intimately related to supercapacitor performance, notably energy storage capacity, power density, and cycle life. Nanomaterials have a high surface-to-volume ratio, which implies they can store more electroactive sites for ion adsorption and allow for faster charge/discharge rates. This makes them ideal for use as electrodes in sophisticated supercapacitors [1–8]. Carbon nanotubes, graphene, and activated carbon are prevalent carbon nanomaterials. EDLCs often use these materials, storing energy by means of physical ion adsorption on their high-surface-area architectures [9,10]. Transition-metal oxides, including Co_3O_4, MnO_2, and NiO, demonstrate pseudocapacitance by storing energy via reversible faradaic processes [11]. Nanostructuring of these oxides

optimizes surface area and reduces diffusion distances, enhancing capacitance and cycle stability [12,13]. A multitude of individuals use conducting polymers such as polyaniline (PANI), polypyrrole (PPy), and polythiophene, which exhibit elevated capacitance via redox mechanisms. Wearable supercapacitors may include polymer nanostructures owing to their flexibility [14–16].

Cobalt oxide (Co_3O_4) has emerged as one of the most promising nanomaterials for supercapacitor applications due to its high theoretical specific capacitance (3560 F g^{-1}), excellent electrochemical stability, and advantageous redox characteristics [17,18]. Co_3O_4 adopts a typical spinel crystal structure in which Co^{2+} ions occupy the tetrahedral interstitial sites, while Co^{3+} ions are located at the octahedral interstitial sites within the cubic close-packed arrangement of oxygen anions [19]. This unique structural configuration imparts Co_3O_4 with advantageous electronic and ionic transport properties, making it an attractive material for energy storage applications. Considerable research efforts are currently directed toward developing efficient synthesis methodologies for fabricating Co_3O_4 nanostructures with diverse morphologies, as these morphological variations can significantly influence their electrochemical characteristics, particularly in supercapacitor applications [20].

A wide range of morphologies, including nanorods [21,22] nanotubes [23,24], nanoflowers [25], and nanowires [26,27], have been reported in the literature, showcasing the adaptability of Co_3O_4 in various structural forms. To achieve these morphologies, multiple synthesis techniques have been employed, such as co-precipitation, sol–gel methods, hydrothermal approaches, solution combustion methods, and colloidal approaches [28,29]. Each of these techniques offers distinct advantages in terms of controlling particle size, surface area, and porosity, which are critical parameters affecting the electrochemical performance of Co_3O_4.

Extensive research has demonstrated the effectiveness of various methodologies in synthesizing Co_3O_4 nanostructures with enhanced functional properties. For example, Kalpana et al. conducted a comparative analysis of the supercapacitive performance of Co_3O_4 nanocrystals fabricated using co-precipitation (Co_3O_4-C) and hydrothermal (Co_3O_4-H) techniques. Both samples exhibited a spinel-type cubic crystal structure and pseudocapacitive behavior. Notably, the hydrothermally synthesized Co_3O_4-H, characterized by a distinctive flower-like morphology, achieved a significantly higher specific capacitance of 366 F/g at a current density of 0.5 A/g compared to the spherical Co_3O_4-C particles, which exhibited a specific capacitance of 233 F/g at 0.5 A/g [25]. Kalyanjyoti et al. synthesized highly stable Co_3O_4 nanocrystals, including 0D nanospheres and 2D hexagonal platelets, through a solvothermal method. The morphology transition from nanospheres to platelets was found to be reaction-time-dependent. Electrochemical analysis revealed that the hexagonal platelets exhibit exceptional capacitive performance, achieving a specific capacitance of 476 F/g at a current density of 0.5 A/g. This superior performance is attributed to their morphology, which enhances ion accessibility. Further improvements in capacitance could be achieved by incorporating large surface area supports or conductive fillers [30]. Co_3O_4 nanoparticles were synthesized by Shwetha et al. using the solution combustion method, with variations in the fuel-to-oxidizer ratio. The electrode produced with a F/O ratio of 1 demonstrated exceptional performance, achieving a specific capacitance of 205 F/g at a scan rate of 2 mV/s, 166 F/g at a current density of 0.5 A/g, and retaining 90% of its capacitance after 5000 cycles. Its uniform particle distribution and high surface area make it a highly promising material for supercapacitor applications [31]. Rose Babu et al. synthesized cobalt oxide nanoparticles hydrothermally at various temperatures and analyzed their structural, optical, and electrochemical properties. The material showed a specific capacitance of 450 F/g at 1 A/g and retained over 88% capacitance over

10,000 cycles at 20 A/g, indicating excellent stability and low charge transfer resistance [32]. The Co_3O_4@N-MWCNT composite was synthesized by Rajendra Kumar et al. through a sonication-assisted thermal reduction process, specifically tailored for enhanced supercapacitor performance. This method facilitated the integration of Co_3O_4 nanoparticles onto nitrogen-doped multi-walled carbon nanotubes, improving both the electrical conductivity and electrochemical stability of the composite. The electrode exhibited an impressive electrochemical capacitance of 225 F/g at a current density of 0.5 A/g [33]. Tao et al. developed a novel flexible Co_3O_4 electrode with an amorphous, hydroxyl-rich structure created through the electrochemical oxidation of a cobalt-based metal–organic framework. The electrode features large micro-rods, small nanoparticles, and abundant mesopores, which enhance electron transfer, active interface exposure, and electrolyte ion penetration. The Co_3O_4 electrode demonstrates a high specific capacitance of 226.1 C/g and excellent rate performance, outperforming crystalline, hydroxyl-deficient Co_3O_4 electrodes [34].

Building on these advancements, the present study focuses on synthesizing Co_3O_4 nanocubes using a facile hydrothermal technique. Potassium hydroxide solution was employed as a reducing agent at varying molar ratios to explore its influence on microstructural and electrochemical properties of materials. Specifically, the synthesis of Co_3O_4 nanocubes via a hydrothermal method and the investigation of KOH as a reducing agent, focus on the impact on the microstructure and electrochemical properties of the materials as electrode candidates for supercapacitors. The as-reported results underscore the potential of this approach for producing high-performance electrode materials tailored for advanced supercapacitor applications.

2. Materials and Methods

2.1. Raw Materials

Sigma-Aldrich (Bangalore, India) provided cobalt(II) nitrate hexahydrate ($Co(NO_3)_2{\cdot}6H_2O$) and polyvinylidene fluoride (PVDF), while Spectrochem Chemicals and Thames-Baker (Mumbai, India) provided potassium hydroxide (KOH) (99%) and N-methyl pyrrolidone (NMP). We utilized all of the compounds directly, without any additional purification. All synthesis methods were carried out using deionized water and ethanol.

2.2. Synthesis Procedure

In a typical synthesis process (Scheme 1), cobalt nitrate hexahydrate and KOH were used as precursors in a stoichiometric ratio. Initially, a 1 M cobalt nitrate solution was prepared in 20 mL of deionized water and stirred for 1 h to ensure homogeneity. Then, 20 mL of 1 M KOH was added dropwise while continuously stirring with a magnetic stirrer for an additional hour. The resulting mixture was transferred to a 100 mL Teflon-lined autoclave, where the reaction was conducted at 200 °C for 24 h. After cooling the autoclave to room temperature, the resulting material was washed and rinsed four times with ethanol and distilled water to remove any impurities. The precipitate was then dried at 80 °C for 5 h and subsequently calcinated at 400 °C for 4 h with a heating rate of 3 °C/min. The sample synthesized with a 1:1 precursor ratio of cobalt nitrate and KOH was designated as COK 11. For comparison, samples prepared with different ratios of $Co(NO_3)_2{\cdot}6H_2O$ and KOH, specifically 1:3 and 1:5 were labeled COK 13, and COK 15, respectively.

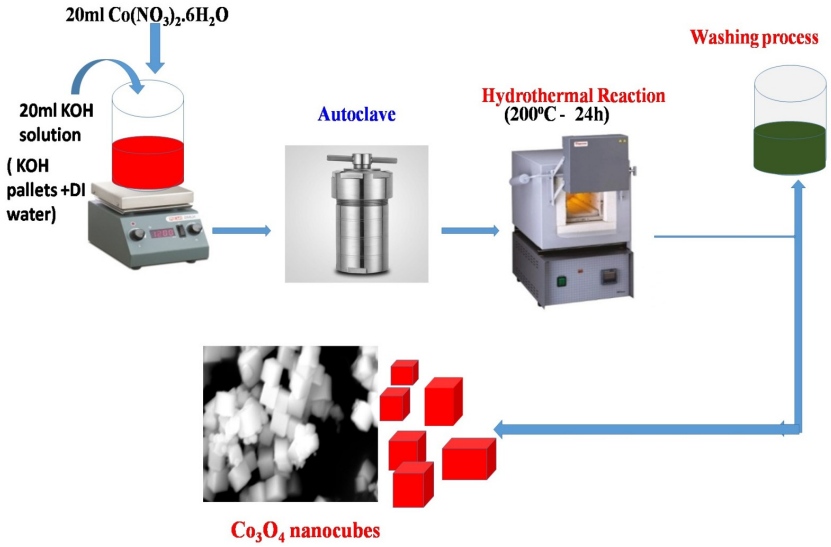

Scheme 1. Illustration of the synthesis of the procedure of cobalt oxide nanoparticles.

2.3. Microstructural and Electrochemical Measurements

The microstructural properties of the Co_3O_4 nanocubes were analyzed using X-ray diffraction (XRD) using a Rigaku miniflex600 apparatus with the CuKα radiation (0.15406 nm). The morphology of the produced cobalt oxide was evaluated using a field emission scanning electron microscope (FE-SEM, Carl Zeiss, Jena, Germany) equipped with energy dispersive X-ray analysis (EDAX) and a high-resolution transmission electron microscope (HR-TEM). The structural changes of porous Co_3O_4 nanocubes were explored using X-ray photoelectron spectroscopy (XPS, Thermo Scientific, Delhi, India) with Al Kα radiation under the pressure of 5×10^{-9} Torr and Fourier transform infrared (FTIR, model IR300, Nicolet, Chennai, India).

The electrochemical performance of the prepared cobalt oxide electrodes was evaluated in a 3 M KOH aqueous electrolyte within a voltage range of 0.0 to 0.5 V at room temperature, using a CHI 608C electrochemical workstation (Instrument Inc., USA) in a three-electrode glass cell. The working electrode was prepared by combining 80 wt.% active material, 10 wt.% PVDF, and 10 wt.% carbon black. After grinding these components for 3 h, a small amount of NMP solution was added to form a smooth slurry. Cleaned nickel foam pieces (1.5 cm^2) were coated with the slurry through a drop-casting technique and dried overnight at 100 °C.

For electrode preparation, commercial nickel foam sheets were cut into 1.5 cm × 1 cm pieces. Some foam pieces were immersed in 3 M hydrochloric acid and then sonicated for 15 min to remove the NiO layer and any residual hydrocarbons on the surface. The cleaned foams were then rinsed with deionized water and ethanol in an ultrasonic bath and dried in a vacuum oven for later use. The electrode's mass loading was 2.02 mg/cm^2. The Ag/AgCl and a platinum strip were used as reference and counter electrodes, respectively.

3. Results and Discussion

3.1. Morphology and Composition

The SEM micrographs shown in Figure 1a–c illustrate the hydrothermal synthesis of COK-11 to COK-15 samples. Cobalt nitrate was used as the precursor and potassium hydroxide (KOH) as both a reducing agent and a morphological control agent. At an equimolar ratio of cobalt nitrate to KOH (COK-11), the resulting particles exhibit a well-defined cubic morphology (Figure 1a). Each cubic particle (Figure 1b) consists of smaller, approximately spherical grains that assemble to form mesoporous networks at

the inter-grain junctions [35,36]. The morphology of the particles undergoes a substantial transformation with variations in KOH concentration. When the precursor-to-reducing agent ratio increases to 1:3 or 1:5, the morphology shifts predominantly to spherical particles (Figure 1c) or agglomerated particle clusters (Figure 1d), respectively. The measured particle size range of the prepared COK 11, COK 13, and COK 15 samples was found to be 200–250, 60–100, and 100–400 nm, respectively.

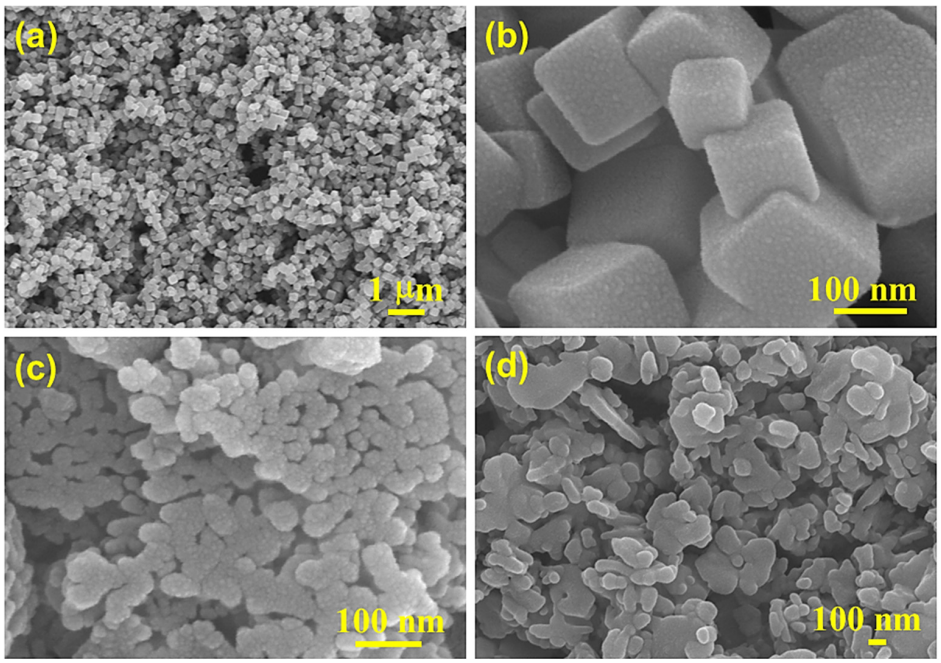

Figure 1. FE-SEM images of COK 11 (**a**,**b**), COK 13 (**c**), and COK 15 (**d**) samples.

Energy dispersive X-ray spectroscopy (EDS) analysis (Figure S1) confirms the elemental composition of the synthesized COK-11 powder, with cobalt (41.20 at.%) and oxygen (58.80 at.%) present at a stoichiometric ratio consistent with the spinel cobalt oxide (Co_3O_4) phase. The elemental mapping of COK-11 also confirms the uniform distribution of cobalt and oxygen throughout the scanning area of the nanocubes, as shown in Figure S2. Conversely, a lower ratio of 1:0.5 yields a heterogeneous mixture of irregularly shaped cubic particles interspersed with scattered grains, as shown in Figure S3.

Transmission electron microscopy analysis (Figure 2) provides additional insights into the morphology and crystallinity of the synthesized COK 11 nanomaterials. Figure 2a,b reveal cubic nanoparticles, corroborating the SEM findings, with an average side length of approximately 250 nm and a calculated volume of 10^6 nm^3. High-resolution TEM (HR-TEM) imaging shows distinct lattice fringes (Figure 2c). The upper and lower insets in Figure 2c display a measured d-spacing of 0.245 nm, corresponding to the (311) crystallographic plane of the spinel Co_3O_4 structure. Furthermore, the uniform spatial distribution of cobalt signals from the L and K shells and oxygen signals from the K shell in line scan (Figure 2d) further validate the successful formation of Co_3O_4 nanocubes, with cobalt atoms in +2 and +3 oxidation states balanced by oxygen in a -2 oxidation state. Also, the size of the nanocubes was found to be 250 nm.

Note that the 1:1 molar ratio was chosen because it produces well-defined cobalt oxide particles with increased electrochemical characteristics. Under supercritical water circumstances, OH^- ions from KOH act as both a reducing and supersaturation-inducing agent, influencing the nucleation and development of cobalt oxide particles. The process includes dissolution and recrystallization, which causes cobalt oxide to precipitate from a homogenous solution via chemical interactions in hydrolyzed metal solutions. The KOH

content has a direct influence on the shape of the produced particles, which in turn affects their electrochemical activity. A comparison of several molar ratios demonstrated that at 0.5 M KOH, cobalt oxide created a heterogeneous mixture of irregularly shaped cubic particles (Figure S3), which might impair homogeneity and electrochemical performance. At 1.0 M KOH, well-defined cubic particles (Figure 1a) were produced, with a balanced shape favorable to increased electrochemical activity. However, increasing the precursor-to-reducing agent ratio to 1:3 or 1:5 resulted in significant morphological changes, with the formation of spherical particles (Figure 1b) or agglomerated particle clusters (Figure 1c), which may lead to lower electrochemical efficiency due to increased particle aggregation.

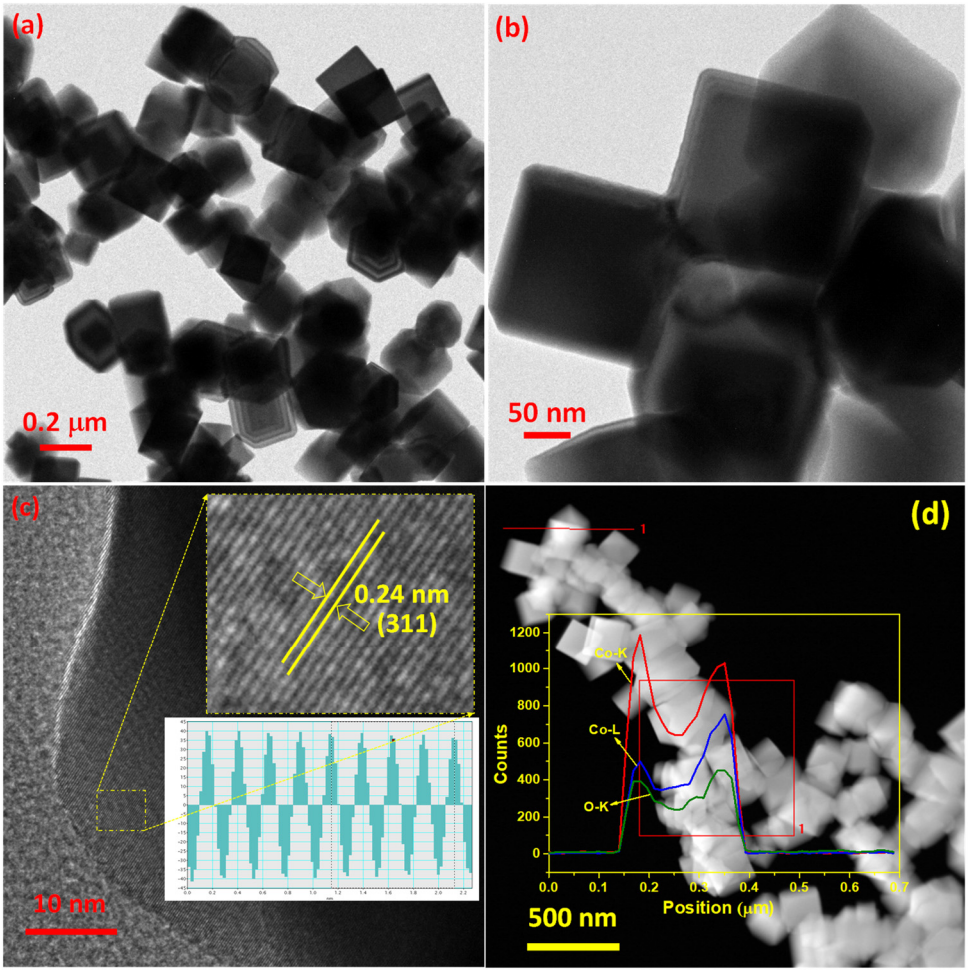

Figure 2. (**a**,**b**) TEM images, (**c**) HRTEM images (top inset: d-spacing between the bright fringes, and down inset: interlayer d-spacing image), and (**d**) STEM and line scan of COK 11 sample.

Furthermore, the linked grains in the cubical particles generated at a 1:1 molar ratio contribute to their porous character, which is critical in electrochemical applications. The COK11 sample had a specific surface area of 38 m^2/g, a pore volume of 0.176 cm^3/g, and a pore diameter of 26 nm, as validated by BET. These holes improve ion transport and electrolyte penetration, hence increasing the material's electrochemical performance. The N_2 adsorption–desorption isotherms of the COK11 sample (Figure S4) indicate the material's porous properties and appropriateness for electrochemical applications due to its high surface area and porosity. Thus, the 1:1 molar ratio was chosen as the best condition because it allowed for the creation of well-defined cubic cobalt oxide particles with an interconnected porous structure, resulting in improved electrochemical characteristics when compared to other molar ratios.

3.2. Structure

The structural properties and phase composition of the synthesized powders were analyzed using X-ray diffraction (XRD), as shown in Figure 3a. Distinct diffraction peaks were observed at angles of 18.8°, 31.1°, 36.6°, 38.4°, 44.6°, 55.5°, 59.2°, 65.1°, and 77.1°, corresponding to the crystallographic planes (111), (220), (331), (222), (400), (422), (333), (440), and (533), respectively. These peaks confirm the formation of Co_3O_4, consistent with previous reports [10,37]. Also, the XRD examination revealed a cubic structure with a space group of *Fd*-3*m*, which corresponds to the data reported on JCPDS card no. 42–1467. The synthesized material displayed moderate crystallinity, as evidenced by the intensity of the diffraction peaks. The calculated lattice parameters $a = b = c = 8.0925$ Å slightly exceed the theoretical value of 8.084 Å. This may be due to nanoscale effects, defect-induced strain, and synthesis conditions. These factors collectively modify the atomic arrangement, leading to a measurable expansion of the unit cell [38]. The average crystallite size (D) of the synthesized samples was estimated using the Scherrer's equation [39,40]:

$$D = \frac{k\lambda}{\beta \cos\theta}, \quad (1)$$

where k is a shape factor with a value of 0.9, λ represents the Cu K_α radiation wavelength, β is the full width at half-maximum (FWHM), and θ represents the Bragg angle. According to this computation, the average crystal sizes of COK 11, COK 13, and COK 15 are 30.6, 24.3, and 21.3 nm, respectively. Additionally, the micro-strain (ε) and dislocation density (δ) values of the obvious peaks were 0.00332 and 1.11×10^{15} for COK 11, 0.00435 and 2.39×10^{15} for COK 13, and 0.00472 and 2.70×10^{15} for COK 15. These values indicate that the crystal size decreases as the ratio increases, and the micro-strain and dislocation density increase. This trend is typical in materials science, whereas smaller crystal sizes often lead to higher strain and dislocation densities due to the increased surface area and defects.

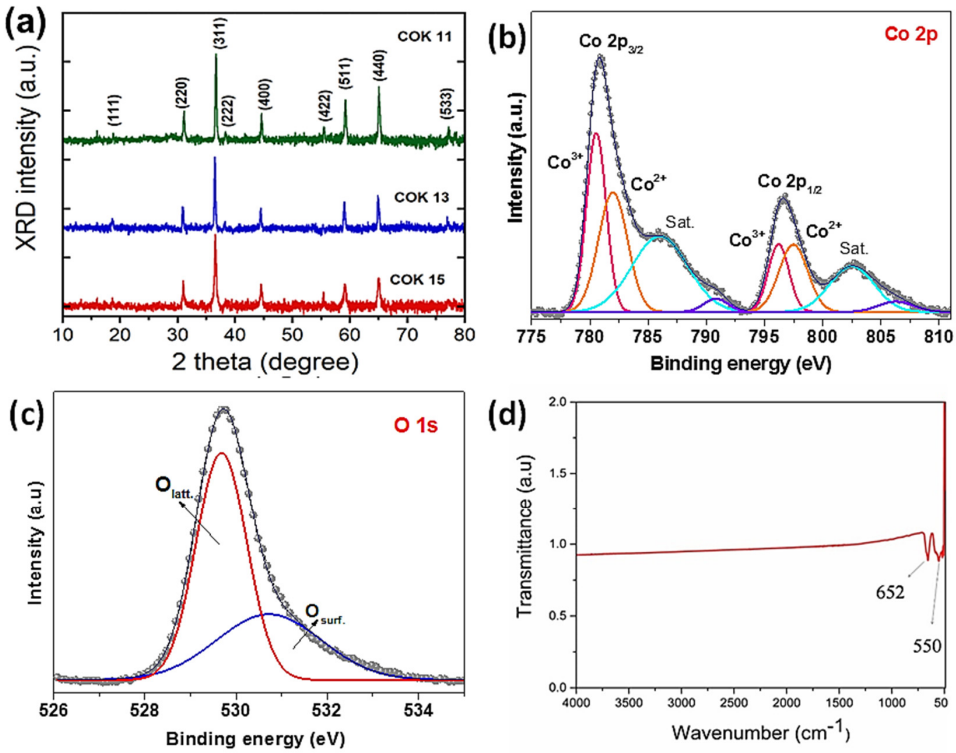

Figure 3. (**a**) XRD spectra of the synthesized cobalt oxide nanoparticles. High-resolution XPS patterns of the Co 2p (**b**) and O 1s (**c**) spectra of the COK 11 sample, and (**d**) FTIR spectrum of the COK 11 sample.

Microstructural results concluded that under supercritical water conditions, the OH^- ions from KOH serve a dual role as both reducing agent and saturation-inducing agents, facilitating the dissolution and recrystallization processes necessary for nucleation. The rapid precipitation of cobalt oxide nanoparticles occurs due to chemical interactions in the homogeneously hydrolyzed metal solutions. The nucleation and growth dynamics are primarily governed by the molar concentration of KOH relative to the cobalt precursor under hydrothermal reaction conditions. At 0.5 M KOH, a mixed morphology of scattered and cubic particles is observed (Figure S1). A uniform cubic morphology develops at 1.0 M KOH (Figures 1a and 2a), whereas aggregated spherical particles dominate at concentrations of ≥3 M KOH (Figure 1c,d). These findings highlight the critical role of KOH concentration in determining particle morphology. The hydrothermal reaction leading to Co_3O_4 formation can be described by Equations (1) and (2), which outline the transformation from dissolved precursors to the crystalline spinel phase.

$$Co(NO_3)_2 + 2KOH \Longleftrightarrow Co(OH)_2 + 2K(NO_3), \quad (2)$$

$$3Co(OH)_2 \xrightarrow{\text{Hy. 210 °C}} Co_3O_4 + 2H_2O. \quad (3)$$

Figure 3b,c show the Co 2p and O 1s XPS spectra. They depict the chemical and valence states at the surface of the COK 11 sample. The peaks at 780.81 and 796.63 eV correspond to Co $2p_{3/2}$ and Co $2p_{1/2}$, respectively, with a spin–orbit splitting of 15.82 eV [41,42]. This demonstrates the Co_3O_4 phase, a common cobalt oxide with mixed Co^{2+} and Co^{3+} oxidation states. The Co $2p_{3/2}$ spectrum is deconvoluted into two peaks at 780.55 and 781.98 eV, attributable to Co^{3+} and Co^{2+} on the surface, and two satellite peaks at 786.0 and 790.83 eV, revealing the distinctive electronic transitions inside cobalt oxides [43]. However, the Co $2p_{1/2}$ spectrum is deconvoluted into peaks at 796.2 and 797.47 eV, corresponding to Co^{3+} and Co^{2+} contributions, followed by satellite peaks at 802.50 and 806.29 eV, verifying the mixed oxidation states [44]. Figure 3c also shows a two-peak O 1s spectrum at 529.67 and 530.72 eV. The peak at 529.67 eV is attributed to lattice oxygen ($O_{latt.}$, O^{2-}), which is inherent in the crystalline structure of Co_3O_4. The signal at 530.72 eV indicates oxygen species adsorbed on surface vacancies (O_{surf}, O^-, $O_2{}^{2-}$, and OH^-) [45,46]. These surface-adsorbed oxygen species are often the result of crystal lattice defects or vacancies, which play an important role in improving the electrochemical characteristics of the materials.

FTIR spectroscopy was employed to analyze the structure of the synthesized Co_3O_4 nanoparticles. Figure 3d shows their FTIR spectrum recorded at room temperature in the 500–4000 cm^{-1} range. Metal oxides generally exhibit characteristic FTIR peaks below 1000 cm^{-1}, attributed to the intra-atomic vibrations. The FTIR spectrum of COK 11 nanoparticles reveals two prominent bands, corresponding to metal–oxygen bonds in its spinel structure. The band at ~660 cm^{-1} is linked to Co^{3+}–O stretching vibrations in octahedral sites, while the band around 550 cm^{-1} is due to Co^{2+}–O stretching in tetrahedral sites. These bands are crucial for identifying the Co_3O_4 phase and align well with the reported data in the literature [47,48].

3.3. Electrochemical Properties

The electrochemical characterizations are performed in optimized 3 M KOH electrolyte. The selection of KOH electrolyte is due to its higher ionic conductivity, smaller hydrated ionic size, and easy ion mobility inside the active electrode materials [49]. Among different alkaline electrolytes, KOH is the most extensive and widely used electrolyte for supercapacitors as a result of high ionic conductivity. KOH is a strong electrolyte as it completely dissociates into K^+ and OH^- ions in an aqueous solution or in the molten state. The very high ionic conductivity is due to the high mobility of the OH^- anion in water

solutions, itself due to its very low size. The specific conductivity of 3 M KOH aqueous solution (0.43 S/cm) is higher than that of 1 M KOH (0.21 S/cm) and more suitable for enhancing the electrochemical properties. In a previous study, the effect of KOH electrolyte concentration on the electrochemical performance of the electrode material was investigated and the optimal concentration of 3 M KOH was identified [50]. Increasing the KOH concentration from 1 M to 3 M enhances ionic conductivity and mobility by providing a higher number of charge carriers. This facilitates redox reactions (oxidation–reduction processes), thereby improving specific capacitance. Additionally, at lower scan rates, ions have sufficient time to diffuse across the electrode–electrolyte interface, further increasing capacitance. Beyond a concentration of 3 M KOH, the capacitance decreased owing to the unusually large quantity of ions, resulting in slow transport kinetics and ion accumulation in the reaction channel. However, higher concentrations of KOH cause corrosion of the electrodes and reference electrodes. Therefore, we chose a moderate concentration of (3 M) KOH to examine the electrochemical properties, similar to the previous reports.

The electrochemical performance of the synthesized cobalt oxide (Co_3O_4) electrodes was systematically evaluated using CV, GCD, and EIS analysis in a 3 M aqueous potassium hydroxide (KOH) electrolyte at ambient temperature. Figure 4a illustrates the current response of the prepared electrode samples, along with a comparison to bare nickel foam, at a scan rate of 60 mV/s within a potential window of 0 to 0.5 V. All tested electrodes exhibited a distinct pair of redox peaks, an oxidative peak around 0.4 V, and a reduction peak near 0.3 V. These peaks correspond to the reversible redox transition between Co^{2+} and Co^{3+} oxidation states during the electrochemical reactions. The following equations can represent these redox processes [31]:

$$Co_3O_4 + OH^- + H_2O \leftrightarrow 3CoOOH + e^-, \quad (4)$$

$$CoOOH + OH^- \leftrightarrow CoO_2 + H_2O + e^-. \quad (5)$$

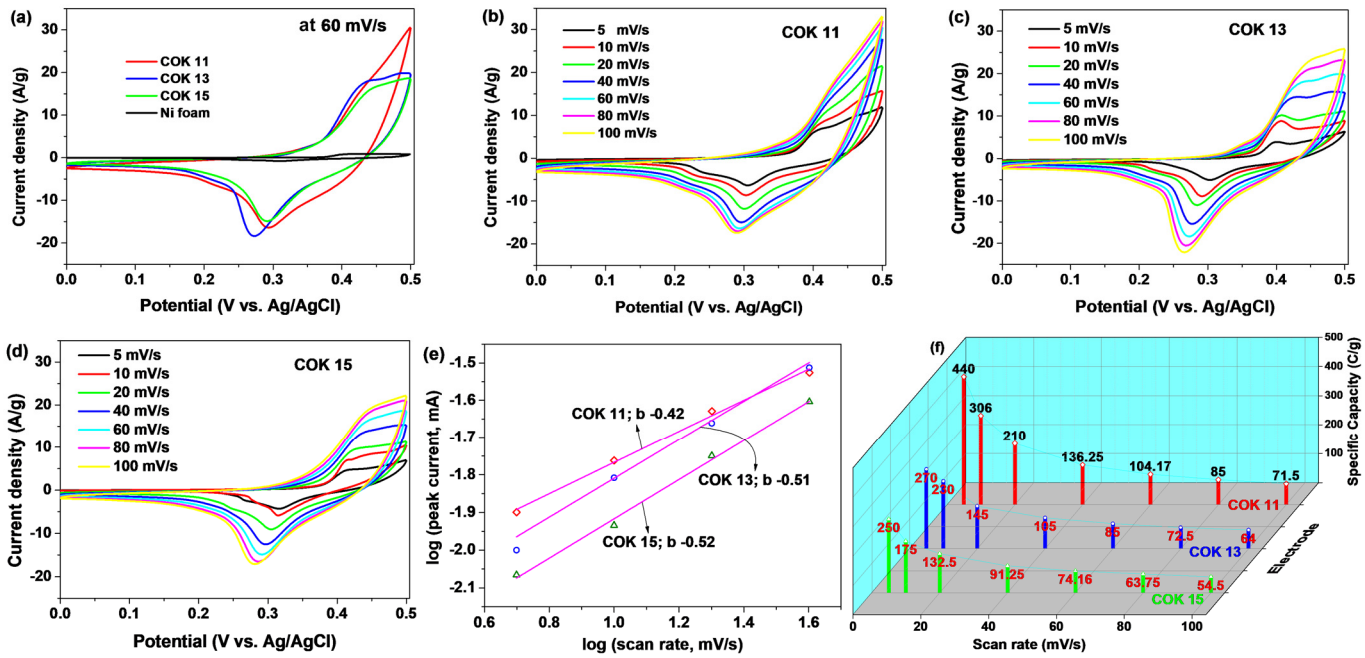

Figure 4. (**a**) Cyclic voltammetry (CV) curves comparing COK 11–15 and bare nickel foam electrodes at a scan rate of 60 mV/s; (**b**–**d**) CV curves of COK 11, COK 13, and COK 15 electrodes recorded at various scan rates (5–100 mV/s), (**e**) log(i_p) vs. log(scan rate) graph; and (**f**) specific capacity values of the COK 11–15 electrodes at corresponding scan rates.

Notably, the COK 11 electrode demonstrated a significantly larger integral area in the CV curve than other samples, suggesting enhanced electrochemical activity. This improvement can be attributed to its unique surface morphology, characterized by nanocubic structures offering abundant electroactive sites and interconnected pores, facilitating efficient ion transport within the electrolyte. Figure 4b–d further confirm that, across all cobalt oxide electrodes, the current response and integral area of the CV curves increased proportionally with the applied scan rate. This behavior highlights the involvement of both surface-controlled and diffusion-controlled redox mechanisms in the charge storage process [51,52]. The relative contribution of these mechanisms was assessed using the power-law relationship ($I = av^b$), where b serves as an indicator of the reaction kinetics [53,54]. For the COK 11–15 electrodes, the calculated b-values ranged from 0.41 to 0.52 (Figure 4e), indicating a predominant diffusion-controlled mechanism occurred during the charge storage process. The specific capacity (Q_{sp}) of the electrode was derived from the CV data using the following equation [53,55]:

$$Q_{sp}\left(Cg^{-1}\right) = \frac{1}{m\nu}\int_{V_i}^{V_f} I(V)dV, \quad (6)$$

where $\int_{V_i}^{V_f} I(V)dV$, represents the integral area of the CV curve, m is the mass of the active electrode material (in mg), and ν is the scan rate (in mV/s). The calculated specific capacities of the COK 11 electrode were 880, 612, 420, 272, 208, 170, and 143 F/g at a scan rate of 5, 10, 20, 40, 60, 80, and 100 mV/s, respectively, as shown in Figure 4f. In comparison, the COK 13 and COK 15 electrodes exhibited lower specific capacities of 540, 460, 290, 210, 170, 144, and 128 F/g, and 500, 350, 264, 182, 148, 126, and 108 F/g, respectively, under the same scan rates.

Among all the electrodes studied, the COK 11 electrode displayed superior specific capacities, corroborating the results of CV measurements and the observed microstructural characteristics. Figure 4f also reveals a general decline in specific capacity with increasing scan rates. This decrease can be attributed to the limited interaction time available between the electrolyte ions and the electrode surface during rapid faradaic reactions, which constrains charge storage efficiency under high scan rates [56,57].

The galvanostatic charge–discharge (GCD) profiles of the cobalt oxide electrodes were recorded at varying current densities within the same potential window used for CV measurements. These GCD curves exhibited voltage plateaus at ~0.4 and ~0.3 V versus Ag/AgCl, consistent with the redox peaks observed in the CV curves. The non-linear shape of the GCD profiles confirmed the battery-type electrochemical behavior of the electrodes. The specific capacity (C_s) of the electrode was calculated using the following formula [58,59]:

$$\mathrm{Cs(F/g)} = \frac{I\,\Delta t}{m}. \quad (7)$$

Figure 5a illustrates the comparative GCD curves of COK 11, COK 13, and COK 15 samples at a current density of 1 A/g. Among these, the COK 11 electrode exhibited longer charge–discharge duration than COK 13 and COK 15, indicating superior charge storage capability. The specific capacities measured at 1 A/g were 825.6, 599.4, and 403.4 F/g for COK 11, COK 13, and COK 15, respectively. GCD profiles for these electrodes at current densities ranging from 1 to 4 A/g are presented in Figure 5b–d. The COK 11 electrode delivered specific capacities of 825, 700, 576, and 468 F/g (uncertainty of ±3 F/g) at current densities of 1, 2, 3, and 4 A/g, respectively. Similarly, the COK 13 electrode achieved capacities of 599, 526, 425, and 338 F/g, while the COK 15 electrode yielded 403, 244, 143, and 104 F/g under the same current densities. These results demonstrate that the COK 11

electrode exhibited the highest rate capability (56.88%), outperforming COK 13 (54.71%) and COK 15 (25.77%).

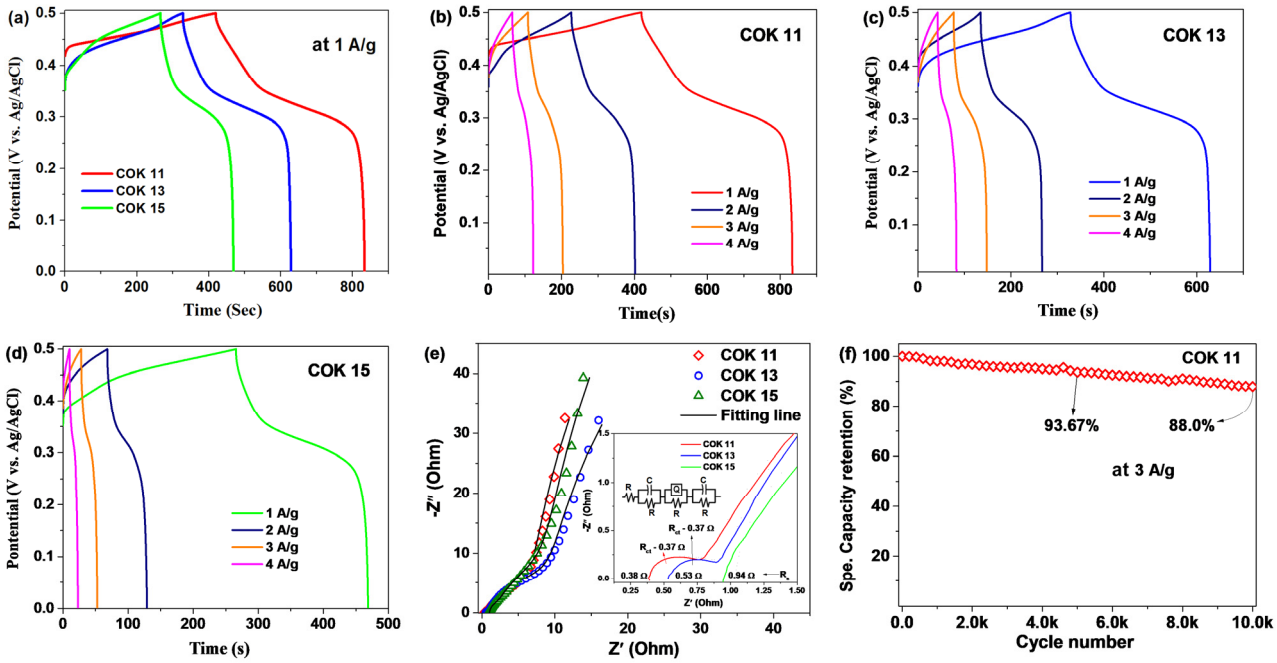

Figure 5. (**a**) GCD curves comparing COK 11–15 electrodes at a current density of 1 A/g; (**b**–**d**) GCD curves of COK 11, COK 13, and COK 15 electrodes recorded at various current densities (1–4 A/g), (**e**) EIS spectra of COK 11–15 electrodes, inset: R(CR)(QR)(CR) equivalent circuit with enlarging Nyquist plots at higher frequency region; and (**f**) cycling stability performance of the COK 11 electrode at a current density of 3 A/g.

Note that recent breakthroughs have focused on creating novel nanostructured electrode materials, including carbon-based materials (10 wt.% carbon black) and hybrid composites, to increase supercapacitor electrochemical performance and scalability [60].

To elucidate the electrochemical reaction kinetics, electrochemical impedance spectroscopy (EIS) was performed (Figure 5e). The Nyquist plots revealed two distinct regions: a high-frequency semicircle and a low-frequency linear tail. The semicircle corresponds to the charge-transfer resistance (R_{ct}) associated with redox reactions between the electrode material and the electrolyte, while the intercept on the real axis represents the equivalent series resistance (R_s). The linear portion at low frequencies indicates the ion diffusion impedance (Warburg impedance, W) [61–63]. All Nyquist plots were well-fitted to an equivalent circuit model R(CR)(QR)(CR) (inset in Figure 5e) with χ^2 values of 2.38×10^{-3} (COK 11), 1.57×10^{-3} (COK 13), and 1.74×10^{-2} (COK 15). The R_s values for COK 11, COK 13, and COK 15 were 0.38, 0.53, and 0.94 Ω, respectively. Similarly, the charge transfer resistance (R_{ct}) values for COK 11 and COK 13 were both 0.37 Ω, indicating the superior electrochemical conductivity of COK 11. Furthermore, the steep linear segment in the Nyquist plot of COK 11 confirmed its excellent ion-diffusion properties. Figure 5f displays the cycling stability of the COK 11 electrode at a current density of 3 A g^{-1}. After 5000 cycles, the specific capacity retention is 93.67%, and after 10,000 cycles, it retains 88% of its initial value, demonstrating exceptional long-term stability and durability. Furthermore, the specific capacity and cycling stability of the COK 11 electrode were compared with those of previously reported cobalt oxide electrodes, as presented in Table 1. The results demonstrate its superior electrochemical performance in a three-electrode system compared to the earlier cobalt oxide electrodes.

Table 1. Comparison of the electrochemical performance of the COK 11 electrode with other recently reported cobalt oxide electrodes in a three-electrode system.

Electrode Material	Electrolyte	Specific Capacity/Capacitance (C/g or F/g)	Current Density (A/g)	Cycling Stability	Ref.
Co_3O_4 nanorod arrays	3 M KOH	154.9 C/g (387.25 F/g)	1	88% after 1000 cycles at 1 A/g	[21]
Hexagonal platelet Co_3O_4 particles	2 M KOH	476 F/g	0.5	82% after 2000 cycles at 2.5 A/g	[30]
Co_3O_4 nanoparticles	2 M KOH	166 F/g	0.5	90% after 5000 cycles at 5 A/g	[31]
Co_3O_4 nanoparticles	3 M KOH	450 F/g	1	88% over 10,000 cycles at 20 A/g	[32]
Co_3O_4@N-MWCNT	3 M KOH	225 F/g	0.5	97.8% after 5000 cycles at 0.5 A/g	[33]
Hydroxyl-rich Co_3O_4	1 M KOH	226.1 C/g	1.3	77% after 5000 cycles at 5 mA cm^{-2}	[34]
CoO/rGO nanocomposite	1 M KOH	592 F/g	2	90% after 3000 cycles at 5 A/g	[64]
ZIF-67-CoO/rGO	6 M KOH	275 F/g	1	--	[65]
AC/Co_3O_4 nanoparticles	1 M Na_2SO_4	182 F/g	1	99.6% over 6000 cycles at 2.5 A/g	[66]
COK 11 or cobalt oxide nanocubes	3 M KOH	825.6 F/g (412.8 C/g)	1	88% after 10,000 cycles at 3 A/g	this work

4. Conclusions

In summary, the hydrothermal synthesis of Co_3O_4 nanomaterials demonstrated that the morphology, crystal structure, and electrochemical properties of the particles are significantly influenced by the concentration of potassium hydroxide. The optimized 1:1 molar ratio of cobalt nitrate to KOH (COK 11) produced well-defined cubic nanostructures with uniform elemental distribution, as confirmed by SEM, TEM, and EDS analyses. The structural characterization through XRD, XPS, and FTIR further validated the formation of the Co_3O_4 spinel phase with characteristic lattice and surface oxygen features. Electrochemical evaluations revealed that the COK 11 electrode outperformed its counterparts in terms of specific capacity and electrochemical activity, attributable to its nano cubic morphology and interconnected porosity, which facilitated efficient ion transport and increased active surface area. The gradual decline in specific capacity with increased scan rates across all samples underscores the diffusion-controlled nature of the charge storage mechanism. The COK 11 electrode demonstrates a high specific capacity of 412 $\pm$ 2 C/g (@ 1 A/g), remarkable rate capability (56.88%), and excellent cycle stability (88%) after 10,000 cycles. It concludes that the critical role of synthesis parameters in tailoring the structural and electrochemical properties of cobalt oxide nanomaterials makes COK-11 a promising candidate for energy storage applications.

Supplementary Materials: The following supporting information can be downloaded at: https://www.mdpi.com/article/10.3390/physchem5010011/s1, Figure S1: EDS spectrum of COK 11 sample; Figure S2: Elemental mapping of COK 11 sample with Co K, and O K elements; Figure S3: FE-SEM image of cobalt oxide sample with 1:0.5 ratio of cobalt nitrite and KOH; Figure S4: N_2 adsorption and desorption isotherms of the COK 11 sample.

Author Contributions: Conceptualization, O.M.H.; formal analysis, B.H. and M.D.; investigation, B.H. and M.D.; data curation, B.H. and M.D.; writing—original draft preparation, M.D. and O.M.H.; writing—review and editing, C.M.J.; supervision, O.M.H. All authors have read and agreed to the published version of the manuscript.

Funding: This research received no funding.

Data Availability Statement: All data are contained in this article or the Supplementary Materials.

Conflicts of Interest: The authors declare no conflicts of interest.

References

1. Yoon, Y.; Truong, P.L.; Lee, D.; Ko, S.H. Metal-oxide Nanomaterials Synthesis and applications in flexible and wearable sensors. *ACS Nanosci. Au* **2022**, *2*, 64–92. [CrossRef]
2. Goyal, M.; Singh, K.; Bhatnagar, N. Applications of nanomaterials for enhanced performance, and sustainability in energy storage devices: A review. *ChemistrySelect* **2024**, *9*, e202400543. [CrossRef]
3. Singh, P.K.; Kaur, G.A.; Shandilya, M.; Rana, P.; Rai, R.; Mishra, Y.K.; Syväjärvi, M.; Tiwari, A. Trends in piezoelectric nanomaterials towards green energy scavenging nanodevices. *Mater. Today Sustain.* **2023**, *24*, 100583. [CrossRef]
4. Saleh, H.M.; Hassan, A.I. Synthesis and characterization of nanomaterials for application in cost-effective electrochemical devices. *Sustainability* **2023**, *15*, 10891. [CrossRef]
5. Al-Mahmud, M.Z. A Concise Review of nanoparticles utilized energy storage and conservation. *J. Nanomater.* **2023**, *2023*, 5432099.
6. Pérez Mendoza, A.E.; Schmidt, A.; Zarbin, A.J.G.; Winnischofer, H. Review of nanoscale approaches for tailoring electrode materials for advanced energy storage systems. *ACS Appl. Nano Mater.* **2024**, *7*, 23295–23320. [CrossRef]
7. Kumar, N.; Kim, S.-B.; Lee, S.-Y.; Park, S.-J. Recent advanced supercapacitor: A review of storage mechanisms, electrode materials, modification, and perspectives. *Nanomaterials* **2022**, *12*, 3708. [CrossRef]
8. Ngidi, N.P.D.; Koekemoer, A.F.; Ndlela, S.S. Recent advancement in the electrochemical performance of electrochemical capacitors based on biomass-derived porous carbon: A review. *J. Energy Storage* **2024**, *89*, 111638. [CrossRef]
9. Waris, M.S.; Chaudhary, A.H.; Anwer, S.; Sultana, P.P.; Ingole, S.A.A.; Nami, M.Z.; Khan, A. Review on development of carbon-based nanomaterials for energy storage devices: Opportunities and challenges. *Energy Fuels* **2023**, *37*, 19433–19460. [CrossRef]
10. Kothandam, G.; Singh, G.; Guan, X.; Lee, J.M.; Ramadass, K.; Joseph, S.; Benzigar, M.; Karakoti, A.; Yi, J.; Kumar, P.; et al. Recent advances in carbon-based electrodes for energy storage and conversion. *Adv. Sci.* **2023**, *10*, 2301045. [CrossRef]
11. Jayakumar, S.; Santhosh, P.C.; Mohideen, M.M.; Radhamani, A.V. A comprehensive review of metal oxides (RuO_2, Co_3O_4, MnO_2 and NiO) for supercapacitor applications and global market trends. *J. Alloys Compd.* **2024**, *976*, 173170. [CrossRef]
12. Pan, J.; Li, C.; Peng, Y.; Wang, L.; Li, B.; Zheng, G.; Song, M. Application of transition metal (Ni, Co and Zn) oxides based electrode materials for ion-batteries and supercapacitors. *Int. J. Electrochem. Sci.* **2023**, *18*, 100233. [CrossRef]
13. Quispe-Garrido, V.; Cerron-Calle, G.A.; Bazan-Aguilar, A.; Ruiz-Montoya, J.G.; López, E.O.; Baena-Moncada, A.M. Advances in the design and application of transition metal oxide-based supercapacitors. *Open Chem.* **2021**, *19*, 709–725. [CrossRef]
14. Tadesse, M.G.; Ahmmed, A.S.; Lübben, J.F. Review on conductive polymer composites for supercapacitor applications. *J. Composites Sci.* **2024**, *8*, 53. [CrossRef]
15. Wang, Y.; Ding, Y.; Guo, X.; Yu, G. Conductive polymers for stretchable supercapacitors. *Nano Res.* **2019**, *12*, 1978–1987. [CrossRef]
16. Alcaraz-Espinoza, J.J.; de Melo, C.P.; de Oliveira, H.P. Fabrication of highly flexible hierarchical polypyrrole/carbon nanotube on eggshell membranes for supercapacitors. *ACS Omega* **2017**, *2*, 2866–2877. [CrossRef]
17. Liao, Q.; Li, N.; Jin, S.; Yang, G.; Wang, C. All-solid-state symmetric supercapacitor based on Co_3O_4 nanoparticles on vertically aligned graphene. *ACS Nano* **2015**, *9*, 5310–5317. [CrossRef]
18. Xu, W.; Li, T.-T.; Zheng, Y.-Q. Porous Co_3O_4 nanoparticles derived from a Co(ii)-cyclohexanehexacarboxylate metal–organic framework and used in a supercapacitor with good cycling stability. *RSC Adv.* **2016**, *6*, 86447–86454. [CrossRef]
19. Wiegmann, T.; Pacheco, I.; Reikowski, F.; Stettner, J.; Qiu, C.; Bouvier, M.; Bertram, M.; Faisal, F.; Brummel, O.; Libuda, J.; et al. Operando identification of the reversible skin layer on Co_3O_4 as a three-dimensional reaction zone for oxygen evolution. *ACS Catal.* **2022**, *12*, 3256–3268. [CrossRef]
20. Velhal, N.B.; Yun, T.H.; Ahn, J.; Kim, T.; Kim, J.; Yim, C. Tailoring cobalt oxide nanostructures for stable and high-performance energy storage applications. *Ceram. Int.* **2023**, *49*, 4889–4897. [CrossRef]
21. Chen, M.; Ge, Q.; Qi, M.; Liang, X.; Wang, F.; Chen, Q. Cobalt oxides nanorods arrays as advanced electrode for high performance supercapacitor. *Surf. Coat. Technol.* **2019**, *360*, 73–77. [CrossRef]
22. Kunhikrishnan, L.; Shanmugham, R. High electrochemical performance of morphologically controlled cobalt oxide for supercapacitor application. *Mater. Character.* **2021**, *177*, 111160. [CrossRef]

23. Xu, J.; Gao, L.; Cao, J.; Wang, W.; Chen, Z. Preparation and electrochemical capacitance of cobalt oxide (Co_3O_4) nanotubes as supercapacitor material. *Electrochim. Acta* **2010**, *56*, 732–736. [CrossRef]
24. More, S.; Joshi, B.; Khadka, A.; Samuel, E.; Il Kim, Y.; Aldalbahi, A.; El-Newehy, M.; Gurav, K.; Lee, H.-S.; Yoon, S.S. Oriented attachment of carbon/cobalt-cobalt oxide nanotubes on manganese-doped carbon nanofibers for flexible symmetric supercapacitors. *Appl. Surf. Sci.* **2023**, *615*, 156386. [CrossRef]
25. Kalpana, S.; Bhat, V.S.; Hegde, G.; Niranjana Prabhu, T.; Anantharamaiah, P.N. Morphology-dependent supercapacitive properties of Co_3O_4 nanomaterials synthesized via coprecipitation and hydrothermal methods. *Inorg. Chem. Commun.* **2023**, *158*, 111458. [CrossRef]
26. Desai, R.S.; Jadhav, V.S.; Morankar, P.J.; Patil, S.B.; Sadale, S.B.; Pardeshi, S.R.; Lad, D.D.; Patil, P.S.; Jeon, C.-W.; Dalavi, D.S. Hydrothermal synthesis of self-supported hierarchical microflowers of Co_3O_4 nanowires for potential supercapacitor application. *J. Electroanal. Chem.* **2025**, *976*, 118800. [CrossRef]
27. Wei, G.; Yan, L.; Huang, H.; Yan, F.; Liang, X.; Xu, S.; Lan, Z.; Zhou, W.; Guo, J. The hetero-structured nanoarray construction of Co_3O_4 nanowires anchored on nanoflakes as a high-performance electrode for supercapacitors. *Appl. Surf. Sci.* **2021**, *538*, 147932. [CrossRef]
28. Waris, A.; Din, M.; Ali, A.; Afridi, S.; Baset, A.; Khan, A.U.; Ali, M. Green fabrication of Co and Co_3O_4 nanoparticles and their biomedical applications: A review. *Open Life Sci.* **2021**, *16*, 14–30. [CrossRef]
29. Lu, C.; Liu, L.; Yang, Y.; Ma, Y.; Luo, Q.; Zhu, M. Recent progress in Co_3O_4-based nanomaterials for supercapacitors. *ChemNanoMat* **2023**, *9*, e202200537. [CrossRef]
30. Deori, K.; Ujjain, S.K.; Sharma, R.K.; Deka, S. Morphology Controlled Synthesis of Nanoporous Co_3O_4 nanostructures and their charge storage characteristics in Supercapacitors. *ACS Appl. Mater. Interfaces* **2013**, *5*, 10665–10672. [CrossRef]
31. Shwetha, K.P.; Manjunatha, C.; Sudha Kamath, M.K.; Vinaykumar; Radhika, M.G.R.; Khosla, A. Morphology-controlled synthesis and structural features of ultrafine nanoparticles of Co_3O_4: An active electrode material for a supercapacitor. *Appl. Res.* **2022**, *1*, e202200031. [CrossRef]
32. Babu, C.R.; Avani, A.V.; Shaji, S.; Anila, E.I. Electrochemical characteristics of Co_3O_4 nanoparticles synthesized via the hydrothermal approach for supercapacitor applications. *J. Solid State Electrochem.* **2024**, *28*, 2203–2210. [CrossRef]
33. Nare, R.K.; Ramesh, S.; Basavi, P.K.; Kakani, V.; Bathula, C.; Yadav, H.M.; Dhanapal, P.B.; Kotanka, R.K.R.; Pasupuleti, V.R. Sonication-supported synthesis of cobalt oxide assembled on an N-MWCNT composite for electrochemical supercapacitors via three-electrode configuration. *Sci. Rep.* **2022**, *12*, 1998. [CrossRef] [PubMed]
34. Tao, Y.; Wu, Y.; Chen, H.; Chen, W.; Wang, J.; Tong, Y.; Pei, G.; Shen, Z.; Guan, C. Synthesis of amorphous hydroxyl-rich Co_3O_4 for flexible high-rate supercapacitor. *Chem. Eng. J.* **2020**, *396*, 125364. [CrossRef]
35. Hao, P.; Peng, B.; Shan, B.-Q.; Yang, T.-Q.; Zhang, K. Comprehensive understanding of the synthesis and formation mechanism of dendritic mesoporous silica nanospheres. *Nanoscale Adv.* **2020**, *2*, 1792–1810. [CrossRef]
36. Quirk, J.; Rothmann, M.; Li, W.; Abou-Ras, D.; McKenna, K.P. Grain boundaries in polycrystalline materials for energy applications: First principles modeling and electron microscopy. *Appl. Phys. Rev.* **2024**, *11*, 011308. [CrossRef]
37. Sun, J.; Wang, H.; Li, Y.; Zhao, M. Porous Co_3O_4 column as a high-performance Lithium anode material. *J. Porous Mater.* **2021**, *28*, 889–894. [CrossRef]
38. Wei, Z.; Xia, T.; Ma, J.; Feng, W.; Dai, J.; Wang, Q.; Yan, P. Investigation of the lattice expansion for Ni nanoparticles. *Mater. Character.* **2007**, *58*, 1019–1024. [CrossRef]
39. Merum, D.; Nallapureddy, R.R.; Pallavolu, M.R.; Mandal, T.K.; Gutturu, R.R.; Parvin, N.; Banerjee, A.N.; Joo, S.W. Pseudocapacitive performance of freestanding $Ni_3V_2O_8$ nanosheets for high energy and power density asymmetric supercapacitors. *ACS Appl. Energy Mater.* **2022**, *5*, 5561–5578. [CrossRef]
40. Nasiri, S.; Rabiei, M.; Palevicius, A.; Janusas, G.; Vilkauskas, A.; Nutalapati, V.; Monshi, A. Modified Scherrer equation to calculate crystal size by XRD with high accuracy, examples Fe_2O_3, TiO_2 and V_2O_5. *Nano Trends* **2023**, *3*, 100015. [CrossRef]
41. Supriya, S.; Das, S.; Senapati, S.; Naik, R. Cu_2Te/CoTe nanoparticles with tuneable bandgaps: Implications for photovoltaic and optoelectronic devices. *Surf. Interfaces* **2024**, *44*, 103823. [CrossRef]
42. Adesuji, E.T.; Guardado-Villegas, E.; Fuentes, K.M.; Sánchez-Domínguez, M.; Videa, M. Pt-Co_3O_4 superstructures by one-pot reduction/precipitation in bicontinuous microemulsion for electrocatalytic oxygen evolution reaction. *Catalysts* **2020**, *10*, 1311. [CrossRef]
43. Cole, K.M.; Kirk, D.W.; Thorpe, S.J. Co_3O_4 nanoparticles characterized by XPS and UPS. *Surf. Sci. Spectra* **2021**, *28*, 014001. [CrossRef]
44. Daza-Gómez, L.; Pérez Salas, K.Y.; Ruiz-Huerta, L.; García Peña, N.G.; Maturano Rojas, V.; Redón, R. Co_3O_4 @SiO_2 3D monolith catalysts, additive manufactured structures for propane oxidation reaction. *ChemistrySelect* **2024**, *9*, e202304849. [CrossRef]
45. Murugesan, R.A.; Chandar Nagamuthu Raja, K.; Devi, N.; Lin, H.-T.; Huang, C.-C.; Jiang, X.-Y.; Li, Y.-Y.; Arthanareeswaran, G.; Ponvijayakanthan, L.; Jaiswal, N.K.; et al. Development of Ni-doped Co_3O_4 oxygen evolution catalysts for anion exchange membrane water electrolysis. *Int. J. Hydrog. Energy* **2024**, *72*, 677–686. [CrossRef]

46. Urgunde, A.B.; Kamboj, V.; Kannattil, H.P.; Gupta, R. Layer-by-layer coating of cobalt-based ink for large-scale fabrication of OER electrocatalyst. *Energy Technol.* **2019**, *7*, 1900603. [CrossRef]
47. Makhlouf, S.A.; Bakr, Z.H.; Aly, K.I.; Moustafa, M.S. Structural, electrical and optical properties of Co_3O_4 nanoparticles. *Superlattices Microstruct.* **2013**, *64*, 107–117. [CrossRef]
48. Al-Senani, G.M.; Deraz, N.M.; Abd-Elkader, O.H. Magnetic and characterization studies of CoO/Co_3O_4 nanocomposite. *Processes* **2020**, *8*, 844. [CrossRef]
49. Mohanty, G.C.; Das, S.; Verma, A. Fabrication of aqueous asymmetric supercapacitor device by using spinel type $(FeCoNiCuZn)_3O_4$ high entropy oxide and green carbon derived from plastic wastes. *Ceram. Int.* **2024**, *50*, 48938–48947. [CrossRef]
50. Kalpana, S.; Bhat, V.S.; Hegde, G.; Anantharamaiah, P.N. Exploring the influence of KOH electrolyte concentration on the electrochemical properties of Co_3O_4-GO nanocomposite. *J. Phys. Chem. Solids* **2024**, *190*, 112019. [CrossRef]
51. Guragain, D.; Zequine, C.; Gupta, R.K.; Mishra, S.R. Facile synthesis of bio-template tubular MCo_2O_4 (M = Cr, Mn, Ni) microstructure and its electrochemical performance in aqueous electrolyte. *Processes* **2020**, *8*, 343. [CrossRef]
52. Yamada, H.; Yoshii, K.; Asahi, M.; Chiku, M.; Kitazumi, Y. Cyclic voltammetry Part 2: Surface adsorption, electric double layer, and diffusion layer. *Electrochemistry* **2022**, *90*, 102006. [CrossRef]
53. Merum, D.; Ambadi, L.N.; Mahammad, H.O.; Pallavolu, M.R.; Goddati, M.; Lee, J.; Al-Asbahi, B.A.; Pitcheri, R.; Banerjee, A.N.; Joo, S.W. Direct growth of cobalt-doped nickel vanadate shelf-like architectures on Ni foam electrodes for solid-state alkaline battery. *J. Alloys Compd.* **2023**, *950*, 169771. [CrossRef]
54. Merum, D.; Arla, S.K.; Radhalayam, D.; Tighezza, A.M.; Mooni, S.P.; Joo, S.W. Garland-structured $Bi_2O_2CO_3$@$Ni(OH)_2$ as a battery-type electrode for high-performance electrochemical energy storage device applications. *J. Energy Storage* **2024**, *99*, 113189. [CrossRef]
55. Thonge, P.N.; Dhas, S.D.; Waghmare, S.D.; Patil, A.H.; Patil, T.M.; Yewale, M.A.; Mendhe, A.C.; Kim, D. Facile hydrothermal synthesis of $NiMn_2O_4$/C nanosheets for solid-state asymmetric supercapacitor and electrocatalytic oxygen evolution reaction. *ACS Appl. Nano Mater.* **2024**, *7*, 18579–18589. [CrossRef]
56. Sanayee, M.; Arvand, M. Synthesis and electrochemical properties of nanocubes Mn_2SnS_3 for high-performance supercapacitors. *Sci. Rep.* **2023**, *13*, 20838. [CrossRef]
57. Merum, D.; Parvin, N.; Vattikuti, S.V.P.; Nallapureddy, R.R.; Pitcheri, R.; Shkir, M.; Manthrammel, M.A.; Banerjee, A.N.; Joo, S.W. Impact of Co-doping on the microstructural and electrochemical features of mesoporous 3D oval–shaped $Ni_{3-x}Co_xV_2O_8$ electrodes for high-performance hybrid supercapacitors. *J. Energy Storage* **2023**, *61*, 106674. [CrossRef]
58. Chen, X.; Zhuang, Y. Sacrificial template synthesis of hollow-structured NiCoP microcubes as novel electrode materials for asymmetric supercapacitors. *Dalton Trans.* **2022**, *51*, 16017–16026. [CrossRef]
59. Sethi, M.; Shenoy, U.S.; Bhat, D.K. A porous graphene–$NiFe_2O_4$ nanocomposite with high electrochemical performance and high cycling stability for energy storage applications. *Nanoscale Adv.* **2020**, *2*, 4229–4241. [CrossRef]
60. Gomez Vidales, A.; Sridhar, D.; Meunier, J.L.; Omanovic, S. Nickel oxide on directly grown carbon nanofbers for energy storage applications. *J. Appl. Electrochem.* **2020**, *50*, 1217–1229. [CrossRef]
61. Dhananjaya, M.; Lakshmi Narayana, A.; Guru Prakash, N.; Rosaiah, P.; Hussain, O.M. Intertwining network structured V_nO_{2n+1}-CNT/GO nanocomposite electrodes for supercapacitors. *Mater. Chem. Phys.* **2019**, *237*, 121825. [CrossRef]
62. Lazanas, A.C.; Prodromidis, M.I. Electrochemical impedance spectroscopy–A tutorial. *ACS Measurement Sci. Au.* **2023**, *3*, 162–193. [CrossRef] [PubMed]
63. Dhananjaya, M.; Guru Prakash, N.; Lakshmi Narayana, A.; Hussain, O.M. Electrochemical performance of nanocrystalline vanadium pentoxide thin films grown by RF magnetron sputtering. *J. Electronic Mater.* **2020**, *49*, 1922–1934. [CrossRef]
64. Selvarajan, R.; Vadivel, S.; Saranya, A.; Baraneedharan, P.; Jayavel, R. Facile synthesis of rGO@ CoO nanocomposites electrode material for photocatalytic hydrogen generation and supercapacitor applications. *Inorg. Chem. Commun.* **2022**, *139*, 109345. [CrossRef]
65. Zha, X.; Wu, Z.; Cheng, Z.; Yang, W.; Li, J.; Chen, Y.; He, L.; Zhou, E.; Yang, Y. High performance energy storage electrodes based on 3D Z-CoO/RGO nanostructures for supercapacitor applications. *Energy* **2021**, *220*, 119696. [CrossRef]
66. Al-Jahdaly, B.A.; Abu-Rayyan, A.; Taher, M.M.; Shoueir, K. Phytosynthesis of Co_3O_4 nanoparticles as the high energy storage material of an activated carbon/Co_3O_4 symmetric supercapacitor device with excellent cyclic stability based on a Na_2SO_4 aqueous electrolyte. *ACS Omega* **2022**, *7*, 23673–23684. [CrossRef]